

# Interactions of ultrashort strain solitons and terahertz electronic two-level systems in photoexcited ruby

Otto L. Muskens and Jaap I. Dijkhuis\*

Debye Institute, Department of Physics and Astronomy, University of Utrecht, P.O. Box 80 000, 3508 TA, Utrecht, The Netherlands

(Received 2 November 2004; published 31 March 2005)

We examine the interaction between coherent, terahertz strain solitons, and the metastable  $29\text{-cm}^{-1}$  electronic two-level systems in photoexcited ruby. A large difference in soliton-induced  $R_2$  luminescence is observed for soliton propagation along the crystallographic  $c$  axis with respect to earlier experiments along the  $a$  direction [Phys. Rev. Lett. **92**, 035503 (2004)], that can be explained by the strong anisotropy of the crystal field interaction strength. The behavior of the soliton-induced population of terahertz two-level systems is further investigated in several configurations and explained successfully in the context of a model of nonlinear propagation of the supersonic soliton packets and their coherent interaction with the two-level medium.

DOI: 10.1103/PhysRevB.71.104304

PACS number(s): 63.20.-e, 62.30.+d

## I. INTRODUCTION

The availability of directional, high-amplitude strain pulses in the ultrafast regime opens up an avenue to dynamical high-pressure experiments on femtosecond timescales. This regime has recently become accessible through high-power, ultrafast optical excitation of a metallic transducer evaporated onto a crystal. Low-temperature propagation of the generated picosecond strain packets over millimeter distance through the crystal has revealed the development of very short, stable acoustic *soliton* pulses.<sup>1</sup> In this evolution, the dynamical balance between acoustic nonlinearity (provided by the lattice anharmonicity) and phonon dispersion is responsible for the formation of the half-cycle strain solitons. Extension to much higher amplitudes, attainable using excitation by amplified laser pulses,<sup>2,3</sup> has resulted in breakup of the initial picosecond strain packet into *trains* of ultrashort solitons, with up to 0.4% strain amplitudes and a spatial width of only several nanometers, corresponding to terahertz phonon frequencies.

An application of fundamental and potentially technological interest forms the manipulation of ultrashort strain pulses using electronic two-level centers. Two-level systems with terahertz resonance frequencies can be found in the electronic shells of certain transition-metal ions that are embedded in the crystal field of a host matrix. It has been shown previously that these centers can be used as a sensitive detector of incoherent terahertz nonequilibrium phonons.<sup>4-7</sup> On the other hand, experiments on the interaction of gigahertz ultrasonic pulses with the electronic ground-state levels of paramagnetic impurity ions have demonstrated a strong analogy between acoustics and coherent optics in two-level media.<sup>8,9</sup>

In this paper, we study the interactions of a terahertz electronic two-level medium with the ultrashort strain solitons. For this purpose, we employ the well-known  $\bar{E}(^2E) - 2\bar{A}(^2E)$  transition of  $\text{Cr}^{3+}$  ions in optically excited ruby (see Fig. 1) as a quantum-mechanical two-level medium at 0.87 THz resonance frequency. As the  $\bar{E}(^2E)$  level is metastable, the density of two-level systems can be simply controlled through the optical pumping cycle. By exposing this system

to trains of ultrashort acoustic solitons, we have already demonstrated coherent, impulsive interactions along the crystallographic  $a$  axis.<sup>10</sup> Here, we present a complete analysis of our results on the excitation of the  $\bar{E}(^2E) - 2\bar{A}(^2E)$  transition by solitons, including propagation along the ruby  $c$  axis. The experiments are explained by a theory of the nonlinear propagation of ultrashort strain solitons in a resonant two-level medium, that will be introduced in the following section.

## II. THEORY

In the description of the interaction of the ultrashort nonlinear solitons with the two-level medium, we consider separately (a) the excitation of a two-level system by a single strain soliton, (b) the effect of a complete soliton train on a two-level system, and (c) the propagation of the solitons through a dense two-level medium.

### A. Impulsive excitation by a single soliton

We consider first the initial step in the interaction between solitons and the two-level medium, namely, the impulsive

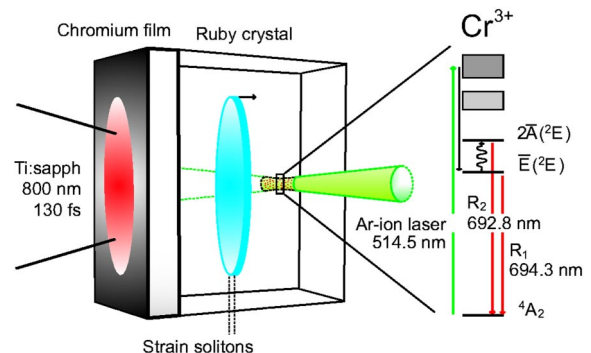


FIG. 1. (Color online) Experimental scheme for generation and detection of coherent strain pulses using the terahertz  $\bar{E}(^2E) - 2\bar{A}(^2E)$  transition in the  $\text{Cr}^{3+}$ -electronic level system. Electronic level system is shown schematically together with the relevant excitation and detection wavelengths.

excitation of an electronic two-level system (TLS) by a *single* ultrashort soliton. The soliton is approximated by a half-cycle pulse of duration  $\tau_s$  with a spectral width  $1/2\tau_s$  larger than the resonance frequency of the TLS  $\nu_0$ . The governing equations for this system are the original Bloch-vector equations, i.e., without the rotating wave approximation<sup>11</sup>

$$\frac{\partial}{\partial t} \mathbf{S} = \boldsymbol{\beta} \times \mathbf{S} - \Gamma(\mathbf{S} - \mathbf{S}_0). \quad (1)$$

Here  $\Gamma$  is the diagonal relaxation matrix describing the dephasing ( $T_2$ ) and energy relaxation ( $T_1$ ) processes in the TLS.  $\mathbf{S}_0$  defines the initial state vector of the electronic levels, and  $\boldsymbol{\beta}$  denotes the pseudofield vector defined as  $[2\chi(t), 0, \omega_0]$ , with  $\chi(t)$  the ‘‘carrier’’ Rabi frequency and  $\omega_0$  the resonant angular frequency of the TLS. The electron-phonon Rabi frequency  $\chi(t)$  depends on the product  $\chi_0 s(t)$  of the pressure coefficient of the crystal-field splitting and the applied strain wave form. For  $\chi_0$  we estimate a value of about  $250 \text{ cm}^{-1}$  per unit strain along the  $a$  axis, as discussed in Appendix A. As usual, the components in the horizontal plane of the Bloch sphere represent the in- and out-of-phase polarizations  $S_1, S_2$ , while the third component  $S_3$  denotes the population difference of the upper and lower states. The quantity of interest for our experiments is the excited-state occupation number  $p_{2\bar{a}}$  defined as  $p_{2\bar{a}} = (S_3 + 1)/2$  (identical to the notation  $\Delta w/2$  in Ref. 10).

As an instructive example we assume that the excitation pulse is much shorter than the resonance period of the TLS, so that the rotation speed in the  $(\hat{S}_1, \hat{S}_2)$  plane is much slower than the vertical tilting of the vector. A simple integration of the system around the passage of a strain pulse  $s(t) = s_0 \text{sech}^2(t/\tau_s)$  then results in a population difference  $p_{2\bar{a}} = 8\chi_0^2 s_0^2 \tau_s^2$ . At typical values for the strain amplitude of 0.4% and corresponding pulse width of 0.2 ps (see Ref. 3), we find an excited-state occupation number of  $p_{2\bar{a}} = 5 \times 10^{-3}$ , corresponding to a tilt of the Bloch vector of  $\sim 8^\circ$ . However, numerical integration of the Bloch equations, including the precession, yields the more accurate value of  $p_{2\bar{a}} \approx 1.2 \times 10^{-3}$  [see Fig. 2(c) discussed later].

### B. Excitation by a soliton train

We proceed by calculating the excitation of the electronic two-level systems using the *full* simulated soliton wave packet<sup>2</sup> including the dispersive tail, as shown in Fig. 2(a). To investigate which parts of the wave packet are resonant with the two-level system, we calculated locally the spectrum by means of successive Fourier transforms over a moving window of 17-ps temporal width. This results in the time-resolved spectrum of Fig. 2(b). The time window for the transform limits the spectral resolution to 60 GHz, which is sufficient to resolve some typical spectral features of the packet. It can be observed that only the first few solitons in the train have frequency components around the TLS resonance at 0.87 THz, denoted by the horizontal line (dash/red). The typical frequency distribution over the wave packet of the trailing tail results from the combined action of the nonlinearity and phonon dispersion, which causes a frequency separation (‘‘chirp’’) in the tail.

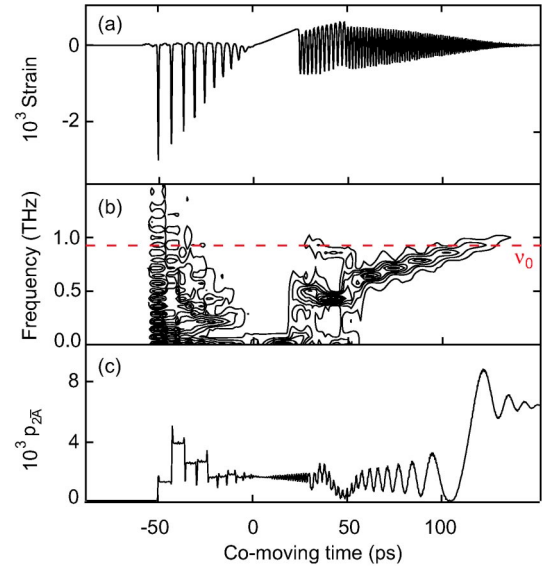


FIG. 2. (Color online) (a) Simulated strain wave packet after  $z \approx 0.5 \text{ mm}$  propagation distance in ruby, for an initial strain  $s_0 = 1.5 \times 10^{-3}$  along the  $a$  axis. (b) Time-dependent Fourier transform of wave form of (a), shown as a contour plot. Horizontal line (red/dash) denotes resonance frequency  $\nu_0$ . (c) Calculated TLS excitation  $p_{2\bar{a}}$  for the simulated wave packet of (a), demonstrating impulsive excitation by the solitons and a resonant contribution from the tail.

We applied the Bloch model to evaluate the action of the wave packet of Fig. 2(a) on a single TLS and obtained the excited-state occupation number  $p_{2\bar{a}}$  from the vertical component of the state vector  $S_3$ . The result, shown in Fig. 2(c), clearly demonstrates the impulsive excitation by the solitons, followed by the resonant character of the excitation by the tail. The excitation efficiency of the total soliton train depends strongly on the distances between subsequent solitons due to the oscillating phase of the TLS. For an average value over an extended crystal volume we have to calculate the excitation of several trains with increasing intervals between the solitons (which has been done in the simulated data of Fig. 5). Furthermore, although the resonant excitation of a single TLS by the tail seems to be higher than that by the solitons, its total contribution in an extended two-level medium will be negligible, due to the different nature of linear and nonlinear propagation that will be the topic of the next section.

### C. Propagation through a two-level medium

The above calculation shows that a bare soliton pulse initially excites a single two-level system to a Bloch angle  $\theta$ . However, when the pulse propagates through a two-level medium, the coherent reemission by the centers results in a trailing tail of resonant radiation,<sup>12–14</sup> which changes the absorption characteristics for a dense medium. In this section we will demonstrate that a fundamental difference exists in the absorption of energy from a nonlinear soliton and a linear strain pulse.

In Ref. 10 we already addressed this point by numerically calculating the refilling of the spectral hole at 0.87 THz by

the nonlinear reshaping of the solitons. Here we go into more detail and demonstrate that the energy extracted by spontaneous emission from the nonlinear solitons is linearly proportional to the amount of absorption centers  $N^*$ , while the energy taken from a linear wave packet by the electronic system is only proportional to  $(N^*)^{1/2}$ . For this purpose we consider subsequently the propagation in the two-level medium of (1) an incoherent phonon spectrum, (2) a coherent linear strain pulse, and (3) a nonlinear soliton pulse.

### 1. Incoherent heat pulse

For an incoherent broad phonon pulse (heat pulse) in a dense medium, the resonant absorption strongly saturates by the depletion of the available  $29\text{-cm}^{-1}$  phonons in the packet. For a Lorentzian resonance line shape, absorption and for that matter spontaneous emission then only takes place in the wings of the resonance, resulting in depletion of a bandwidth  $\Delta$  approximately given by the far-wing expansion of the Lorentzian as

$$\Delta \approx \left( \frac{\Gamma^2 z}{l_r \ln 2} \right)^{1/2}, \quad (2)$$

which for a resonant absorption length  $\bar{l}_r$  inversely proportional to  $N^*$  (see Appendix A) increases with  $(N^*)^{1/2}$ . The amount of energy that is absorbed out of a sufficiently broad phonon spectrum after several resonant mean free paths is thus given by the integral of the phonon density of states  $\rho(\omega_0)$  over the absorption bandwidth  $\Delta$ , times the resonant phonon energy  $\hbar\omega_0$ .

### 2. Coherent linear pulse

We now consider the evolution of a very short (i.e., short compared to  $\pi/\omega_0$ ), coherent linear strain pulse traveling through a two-level medium. This evolution has been thoroughly analyzed for optical radiation propagating in a resonant medium,<sup>12–14</sup> and is analogous to the electron phonon system under study.<sup>8</sup> For small excited-state population, the radiation emitted coherently by the two-level systems accumulates in the form of a superradiant tail [shown in Figs. 3(d)–3(g)]. In this limit, the propagation equation reduces to the dielectric response model and Beer's law (area theorem).<sup>11,12</sup> The combination of the ultrashort pulse and the superradiant tail produces a spectral hole of spontaneously emitted radiation with a bandwidth given by Eq. (2).

The redistribution of energy from the short pulse to coherent and incoherent radiation is illustrated by numerical calculations presented in Fig. 3. We have chosen to describe the wave packet evolution in the spectral domain using the linear response functions (dispersion) of a resonance. For the Lorentzian resonance line shape, the evolution operator  $\tilde{F}(\omega, z)$  has the following spectral form:<sup>11,15</sup>

$$\tilde{F}(\omega, z_j) = \exp[i\tilde{\phi}(\omega)z_j],$$

$$\tilde{\phi}(\omega) \approx \frac{\Gamma}{2} \left( \frac{1}{\omega - \omega_0 - i\Gamma} + \frac{1}{\omega + \omega_0 - i\Gamma} \right), \quad (3)$$

where the propagated distance  $z_j$  is expressed in units of resonant absorption lengths  $z_j = z/\bar{l}_r$ . The complex phase

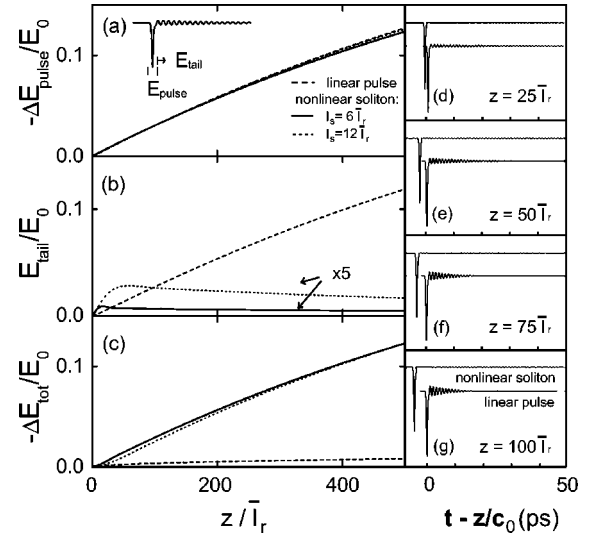


FIG. 3. Dependence on propagated distance  $z/\bar{l}_r$  of (a) energy removed from soliton  $-\Delta E_{\text{pulse}}$ , (b) energy emitted into the superradiant tail  $E_{\text{tail}}$ , and (c) energy removed by spontaneous emission,  $-\Delta E_{\text{tot}}$ , normalized to the initial pulse energy  $E_0$ , for a nonlinear soliton pulse with walk-off length  $l_s=6\bar{l}_r$  (line),  $l_s=13\bar{l}_r$  (short dash), and for a linear strain pulse (dash), i.e.,  $l_s \rightarrow \infty$ . (d)–(g) Snapshots of the simulated propagation of both a linear pulse and a nonlinear soliton ( $l_s=6\bar{l}_r$ ) through the two-level medium.

$\tilde{\phi}(\omega)$  is defined such that its imaginary part equals unity at resonance and Eq. (3) reduces to Beer's law.

Using this response function, we have simulated the propagation of a short linear pulse through the TLS medium over a distance of  $z_j=500$  [dashed line in Figs. 3(a)–3(c)]. Given the estimate of  $\bar{l}_r \approx 2 \mu\text{m}$  of the Appendix, this simulated distance corresponds to about one millimeter of propagation in a ruby crystal with  $N^* = 10^{18} \text{cm}^{-3}$ .

In the simulation we monitor the redistribution of energy from the ultrashort strain pulse into coherent and incoherent relaxation channels by the two-level medium. For this purpose, energy densities are defined locally in the time domain by integration of the square of the coherent strain field over the temporal windows that can be assigned to the soliton pulse and to the trailing radiation packet, respectively [see inset in Fig. 3(a)]. In this way, the energy taken from the pulse by the two-level medium  $-\Delta E_{\text{pulse}}$  and the amount given back coherently in the form of a superradiant tail  $\Delta E_{\text{tail}}$  may be computed and compared with the energy contained in the strain field before entering the TLS medium  $E_0$ . Finally, the difference between these two energies yields the energy removed by spontaneous emission  $-\Delta E_{\text{tot}}$ , which is the quantity detected in our experiments (see Sec. II D).

In Fig. 3(a) we plot  $-\Delta E_{\text{pulse}}/E_0$ , the energy that is removed from the short pulse normalized to the initial pulse energy  $E_0$ , versus propagated distance in the resonant medium. We observe a continuous drain of energy from the short pulse proportional to the traveled distance  $z$ , due to the impulsive excitation of the electronic system. Up to 12% of the initial energy is removed from the pulse over a distance of 500 resonant absorption lengths  $\bar{l}_r$ .

### 3. Coherent nonlinear soliton pulse

In our calculations we also consider the *nonlinear* propagation regime (solid line and dotted line) by simply adjusting the soliton velocity in the moving frame system. The degree of nonlinearity is defined by a walk-off length  $l_s$ , the traveled distance the soliton needs to overtake a linear 0.87-THz phonon by 1/4 of its wavelength. For example, a value of  $l_s = 6\bar{l}_r$  corresponds to a displacement of the soliton over 5.6 ps in the moving frame after one hundred absorption lengths through the crystal [see Fig. 3(g)].

Figure 3(a) shows no difference in the energy drain  $\Delta E_{\text{pulse}}$  from the linear and nonlinear pulses, indicating that the impulsive excitation of two-level systems is not affected by the nonlinear propagation of the solitons. The fundamental difference between linear and nonlinear propagation occurs in the *distribution* of the impulsively excited electronic population over the coherent and incoherent decay channels, as shown in Figs. 3(b) and 3(c). In Fig. 3(b) we plot the energy contained in the coherent resonant radiation  $\Delta E_{\text{tail}}$ . Clearly, in the *linear* case (dashed line), the energy taken from the soliton pulse is almost completely returned to the coherent strain field in the form of trailing radiation. In the time domain this corresponds to the development of a tail with a duration corresponding to the superradiant decay time  $T_R \ll T_2$ ,<sup>12,14</sup> as can be seen in the typical time-domain traces of Figs. 3(d)–3(g). In the spectral domain this corresponds to the development of a spectral hole in the phonon pulse (hole burning).

In contrast, for the *nonlinear* soliton pulse (solid line and dotted line), the amount of energy carried by the trailing radiation tail remains on a very low, stationary level, that is already established after several walk-off lengths  $l_s$ . This stationary state depends on the magnitude of  $l_s$  with respect to  $\bar{l}_r$ . The suppression of energy flow to coherent radiation in the case of nonlinear pulses corresponds to *destructive* interference of the superradiant emission by the walkoff of the soliton, which can also be observed in the traces of Figs. 3(d)–3(g). This destructive interference prevents the development of a spectral hole in the phonon pulse.

The fraction of the total energy  $\Delta E_{\text{tot}}/E_0$  that is converted to the incoherent decay channel via spontaneous emission of the TLS, is shown in Fig. 3(c). Here we find that indeed the energy taken from the nonlinear soliton is completely converted to incoherent emission. Only a minor part of the energy of the linear pulse has been transferred to spontaneously emitted phonons. This part is proportional to  $(N^*)^{1/2}$ , as expected from the absorption bandwidth of Eq. (2). The calculated amount of energy dissipated in the form of spontaneous emission is virtually the same for the two specified values of the walk-off parameter  $l_s$ . This is due to the occurrence of a stationary state of the coherent tail after a propagation over a few walk-off distances. Energy balance *requires* that the constant drain of energy from the soliton is completely transferred to spontaneous emission, irrespective of the magnitude of  $l_s$ .

#### D. Interpretation of the model

In the spectral domain, the frustrated decay channel for the polarization in the nonlinear situation leads to the ab-

sence of a spectral hole in the nonlinear situation, from where a continuous spontaneous emission can take place, proportional to the number of centers  $N^*$ . This refilling takes place due to the mutual coupling of spectral modes by the nonlinear term in the KdV equation.<sup>3</sup> The refilling is governed by the equation for the individual, time-dependent (complex) spectral strain components  $\tilde{s}_k(t)$

$$\frac{\partial \tilde{s}_k(t)}{\partial t} + \alpha \tilde{s}_k(t) \int dk' \tilde{s}_{k'}(t) ik' e^{ik'y} - \beta ik^3 \tilde{s}_k(t) = \tilde{F}(k/c_0, t) \tilde{s}_k(t). \quad (4)$$

Here the subscript  $k$  denotes the wave vector, and  $\alpha$  and  $\beta$  are the nonlinear and dispersive material constants, respectively, of the  $\text{Al}_2\text{O}_3$  host matrix. The right-hand term describes the evolution by the two-level medium, given by Eq. (3). A more accurate description involves the solution of the above KdV equation in the presence of a two-level medium. We did this for one value of the acoustic strain and TLS concentration and obtained the same results as those shown in Fig. 3. In the limit of weak dissipation and low excited-state populations, therefore, our simple model reproduces well the physics of the system, and the nonlinearity can be accounted for through the velocity difference of the soliton and linear phonons.

As mentioned above, in the experiment we are sensitive to the fraction of the energy transferred to spontaneous emission. It is this fraction namely that is resonantly trapped inside the optically excited volume over microsecond time scales<sup>4,7</sup> and brings us the soliton-induced  $R_2$  luminescence signal. As the nonlinear mechanism transfers the total excited population to spontaneously emitted phonons, the amplitude of the  $R_2$  luminescence signal normalized to  $N^*$  will be a direct measure for the impulsively excited population (except for some efficiency factors, see Sec. IV C).

As a final remark, we note that the nonlinear refill mechanism will be ineffective for the low-amplitude dispersive part of the wave packet of Fig. 2 and a spectral hole will be formed similar to the case of a linear pulse. Thus, after the first few resonant mean free paths, the absorption of radiation from the dispersive tail stops, while the soliton train continues to feed 29-cm<sup>-1</sup> phonons via spontaneous emission to the bottlenecked phonon cloud. We therefore assume that in our experiments, where propagation takes place over many Beer's lengths, coherent excitation by the radiative tail may be safely neglected with respect to the excitation by the soliton train.

## III. EXPERIMENTS

### A. Sample and setup

In this section we present experiments conducted in the configuration in which the strain packets propagate along one of the axes of a ruby crystal containing 500 ppm  $\text{Cr}^{3+}$  ions (see Fig. 1 for an impression of the experimental arrangement). For this purpose, the  $9.8 \times 10 \times 15\text{-mm}^3$  specimen was covered with a 100-nm chromium transducer on either one of the  $10 \times 15\text{-mm}^2$  or  $9.8 \times 10\text{-mm}^2$  surfaces, oriented perpendicular to the crystallographic  $c$  and  $a$  axes, re-

spectively. The metastability of the  $\bar{E}(^2E)$  level allows for a continuous adjustment of the TLS density through the excited-state concentration  $N^*$ . This is done by indirect excitation via the broad  $^4T_2$  and  $^4T_1$  absorption bands, using a multimode 2-W argon-ion laser beam focused to a pencil of about  $200\ \mu\text{m}$  in diameter. Excitation of high-amplitude strain pulses takes place via absorption in the metal film of ultrafast optical pulses from an amplified Ti:sapphire laser. The time evolution of the  $R_1$ - and  $R_2$ -emission lines in the crystal is monitored using a double monochromator equipped with a time-resolved photon counting setup. Direct feeding of the  $2\bar{A}(^2E)$  level via the optical pumping cycle is switched off during the acquisition of the soliton signal by means of an acousto-optic modulator. An external magnetic field can be applied in order to lift the degeneracy of the electronic doublets  $\bar{E}(^2E)$  and  $2\bar{A}(^2E)$ , and decrease the bottleneck decay time (see Sec. IV A for details).

### B. Strain pulses traveling along the $c$ axis

Our first set of experiments explores the intensity of the  $R_2$  luminescence in the crystal for propagation of the strain pulses along the  $c$  axis. Our earlier experiments<sup>10</sup> along the ruby  $a$  axis demonstrated strong interaction between strain solitons and the electronic system throughout the entire crystal. However, for propagation along the  $c$  axis, no soliton-induced  $R_2$  luminescence could be detected inside the crystal. The absence of  $R_2$  luminescence induced by the longitudinal phonons can be well understood from the complete disappearance of the matrix element of the single-phonon transition along this symmetry axis.<sup>7</sup>

However, a clear soliton-induced contribution was observed at the far-end of the crystal, near the surface.<sup>16</sup> Trace 1 of Fig. 4 shows the typical time-resolved luminescence intensity as observed either on the propagation axis (line/red), or with a vertical displacement of 1 mm (dash/blue). The peak at zero time and the luminescence background during the first microsecond are due to spurious effects induced by pump light leaking through the metal film. The on- and off-axis signals markedly differ at the time span corresponding to the arrival of LA phonons from the transducer. The maximum amplitude of the effect amounts to  $0.7 \times 10^{-4}$  and critically depends on the intensity of the femtosecond pump laser, shown in Fig. 5. This directly shows that the excitation is critically dependent on the availability of 0.87-THz frequency components in the soliton spectrum and thus on the ultrashort time duration of the incident strain pulses. Together with the directionality of the beam (see the arguments in Ref. 16), this demonstrates that this additional luminescence is induced by the strain solitons.

The soliton-induced  $R_2$  luminescence turns out to be the maximum when the excited zone is positioned just inside the crystal, i.e., close to and partially overlapping with the edge of the crystal [see Fig. 4(a)]. We measured the drop of this signal when scanning the beam into the bulk of the crystal as well as beyond the crystal [see Fig. 4(b)], and find a strong decay within 0.2 mm, the diameter of the excited pencil, followed by a slow attenuation up to  $\sim 1$  mm from the surface. Three typical time-resolved traces [denoted by points 1,

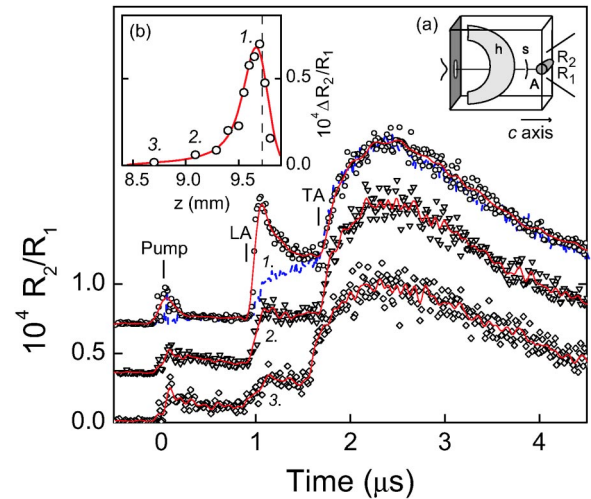


FIG. 4. (Color online) Time-dependent traces of the  $R_2$  luminescence normalized to  $R_1$  at indicated positions in the crystal, (line/red) five-point signal average, (dash/blue) off-axis luminescence intensity. (a) Experimental configuration, with detection region A, soliton pulse  $s$  and heat pulse  $h$ . (b) Soliton-induced  $R_2/R_1$  ratio as a function of position  $z$  in the crystal, (○) experimental data, (line/red) model calculation for diffusive scattering. Vertical line (dash) denotes exact surface position.

2, and 3 in Fig. 4(b)] show that the onset of the LA component becomes less pronounced at increasing distance from the crystal surface. Close inspection shows that the peak in the luminescence signal shifts to *later* times when moving into the crystal, and presumably corresponds to the arrival of phonons reflected from the crystal surface.

The pronounced decay of the soliton-induced luminescence signal into the crystal has been successfully explained by us in a recent paper<sup>16</sup> using a model based on the diffusive scattering of terahertz phonons at the surface of the crystal [line in Fig. 4(b)]. Clearly, the origin of the signal cannot be nonlinear refilling of the spectral hole, introduced in Sec. II C, as the soliton coherence is distorted on the nanometer

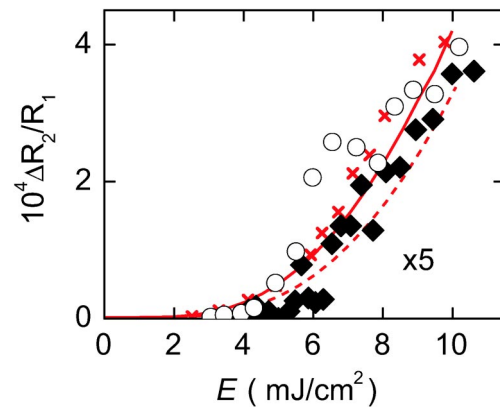


FIG. 5. (Color online) Dependence of soliton-induced  $R_2/R_1$  ratio on pump fluence  $E$ , for propagation along the  $c$  axis (♦) and  $a$  axis (○). (×/red) denotes fit to  $a$ -axis data using Bloch vector model of Sec. II A, and (line, dash/red) denote fits using the square of the 0.87-THz Fourier components in the soliton trains, for values of  $s_0$  calibrated to  $E$  using independent Brillouin data.

scale by reflection at the rough surface. Surface scattering effectively “freezes in” the acoustic spectrum of the soliton as it was present prior to the scattering at the surface. The interaction with the electronic states then should be considered similar to that of an incoherent phonon spectrum and should behave accordingly, i.e., similar to a heat pulse. A more detailed analysis will be presented in Sec. IV.

### C. Strain pulses traveling along the $a$ axis

The configuration in which the strain pulse travels along the  $a$  axis yields a completely different behavior than that observed along the  $c$  axis. Most importantly, along the  $a$  axis, the highly directional soliton maintains a constant luminescence intensity throughout the crystal. The threshold in the pump dependence (see Fig. 5), however, is virtually the same for both configurations, apart from a slightly lower critical pump fluence in the  $a$  axis configuration. This can be explained by the higher nonlinear constant  $\alpha$  in this direction in the crystal,<sup>17</sup> resulting in the generation of terahertz components in the soliton trains already at lower strain amplitudes. The presence of a threshold in the pump-power dependence shows that the excitation depends critically on the availability of 0.87-THz frequency components in the soliton spectrum and can be explained [( $\times$ /red) in Fig. 5] using the coherent Bloch model for the excitation of the TLS by the ultrashort soliton train, while assuming a direct funneling from the impulsive excitation to incoherent  $29\text{-cm}^{-1}$  phonons (see Sec. II C). The presence of a threshold also in the  $c$  axis measurements suggest however that a simple analysis of the amplitude of 0.87-THz frequency components will already yield the observed behavior. We checked this using the analytical expressions for soliton trains of Ref. 3 and the calibrated strain values taken from the Brillouin experiment and find indeed the offset for the resonant spectral component [(line,dash/red) in Fig. 5]. This demonstrates that the threshold in the pump-power dependence is only an indicator for the presence of the 0.87-THz frequency components and does not necessarily contain information on the impulsive nature of the soliton-TLS interaction.

In an additional series of experiments, discussed earlier in Ref. 10, we find that the soliton-induced luminescence behaves fundamentally different than the heat-pulse induced luminescence. Our first observation is that the soliton, in contrast to the heat pulse, survives the passage through a cloud of excited  $\text{Cr}^{3+}$  ions, denoted as zone  $B$  in Fig. 6(a). We analyze this into more detail and present in the experimental traces of Fig. 6 the behavior of the time-resolved  $R_2$  luminescence originating from zone  $A$  after traversing zone  $B$  [see Fig. 6(a)] with indicated excitation densities of zone  $B$ . It is observed that the amplitude of the TA heat-pulse signal decreases with increasing concentration  $N_B^*$  of zone  $B$ , while the soliton-induced LA signal remains unaffected. The behavior of the heat pulse signal can be fit using Eq. (2), that predicts absorption of phonons in the detector zone  $A$  over a bandwidth  $\Delta$  proportional to the square root of its TLS concentration  $N_A^*$ . The secondary zone captures phonons over an absorption bandwidth  $\Delta_B$  and thus reduces the luminescence originating from zone  $A$  by a factor  $\gamma$  given by

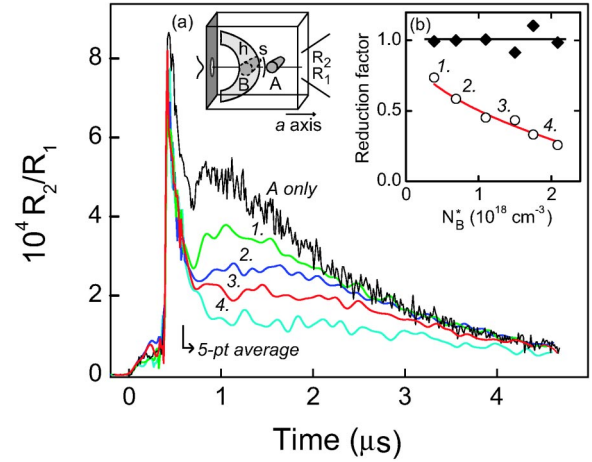


FIG. 6. (Color online) Time-dependent traces of the  $R_2$  luminescence normalized to  $R_1$ , at indicated values (1–4) of  $N_B^*$ , and (line/black) in absence of zone  $B$ . (a) Experimental configuration, with detection region  $A$  and secondary depletion zone  $B$ . (b) Reduction factor for luminescence intensity in presence of zone  $B$ , ( $\circ$ ) TA heat pulse, ( $\blacklozenge$ ) LA soliton. (line/red) Calculation of  $\gamma(N_B^*)$  of Eq. (5).

$$\gamma(N_B^*) = 1 - (N_B^*/N_A^*)^{1/2}, \quad (5)$$

for a TLS concentration  $N_A^* > N_B^*$ . The  $N^*$  dependence of the TA depletion in Fig. 6(b) has been fit to this formula [line in Fig. 6(b)] and therefore is consistent with the simple model for the heat pulse spectrum of Sec. II C.

The insensitivity of the soliton-induced signal for the presence of an additional excited zone demonstrates that the soliton mean free path for absorption by resonant TLS is much larger than the zone dimension of 0.2 mm. This is consistent with the model in which the spectral hole is constantly replenished and the spontaneous emission is linearly proportional to the total number of interacting resonant centers.

The mean free path of the nonlinear solitons in highly excited ruby ( $N^* \sim 10^{18} \text{ cm}^{-3}$ ) was determined using the configuration consisting of an excited pencil *colinear* with the propagating solitons. Figure 7 shows the decay of the soliton-induced signal for three representative values of the TLS concentration of the zone  $N^*$ . The decay length of 7 mm for the highest concentration compares well to the fraction of energy taken from a single soliton by the  $\text{Cr}^{3+}$  centers, assuming a Bloch angle of several degrees. Further, the presented curves display two general properties: (i) the luminescence ratio at the beginning of the sample increases with increasing  $N^*$  and (ii) the soliton mean free path  $\bar{l}$  decreases with increasing  $N^*$ . The first observation, shown into more detail in Fig. 7(a), turns out to correspond well to the  $N^*$  dependence observed for a small excited zone (see Fig. 9) discussed later.

The reduction of the soliton mean free path  $\bar{l}$  with increasing TLS concentration  $N^*$  is explained quantitatively using the spectral response model of Sec. II C. Assuming a rapid refilling and stationary population of the resonant frequency component, a resonant absorption length  $\bar{l}_r$ , inversely propor-

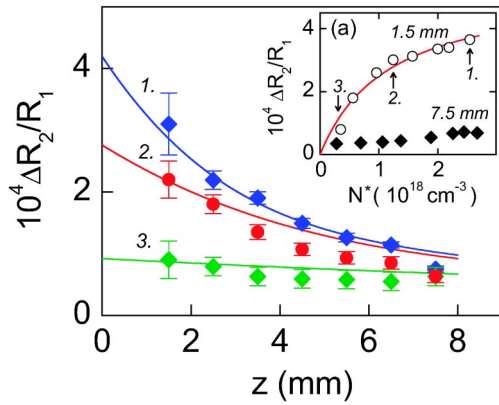


FIG. 7. (Color online) Decay of the soliton-induced luminescence signal in a colinear excited zone, for three values of the concentration  $N^*$  [numbers in (a)] at a pump fluence of  $E \sim 8 \text{ mJ/cm}^2$ . (a) Dependence of luminescence intensity after propagation of 1.5 and 7.5 mm in the excited pencil. (line/red) denotes fit to Eq. (6).

tional to  $N^*$ , can be used to fit the data of Fig. 7. After normalization of the amplitudes and at the highest  $N^*$  we obtain good agreement for a resonant absorption length of  $l_r \approx 1 \mu\text{m}$  (i.e., a simulation over  $z_j = 8000$  resonant absorption lengths) and correspondingly scaled values for the lower concentrations (lines in Fig. 7). Thus the experimentally observed decay of the soliton-induced luminescence at different concentrations  $N^*$  is quantitatively explained using the nonlinear refill model of Sec. II C.

#### IV. INVESTIGATION OF THE SOLITON-TLS INTERACTION

Up to this point, we have discussed two experiments in which the strain packets were traveling along either one of the crystallographic  $a$  (Sec. III C) or  $c$  (Sec. III B) axes. We identified soliton-induced interactions and demonstrated effects of mode conversion at the crystal surface. In Sec. III B, it was already mentioned that there should be a marked difference of the soliton-induced luminescence between the two configurations, as for direct detection the solitons behave essentially nonlinear, while after reflection and mode conversion the wave-packet spectrum and propagation rapidly become linear. In order to make the case more strongly and draw definitive conclusions on the electron-phonon interaction mechanism for the soliton trains, we performed some additional experiments in the two configurations. First, we present the behavior of the soliton-induced luminescence as a function of the applied magnetic field and the TLS density  $N^*$  in Secs. IV A and IV B, respectively. The differences between the *direct* soliton-induced luminescence and that *after* surface scattering will subsequently be discussed in Sec. IV C, based on the coherent interaction model of Sec. II C.

##### A. Magnetic field dependence

The dependence of the decay of bottlenecked 29-cm<sup>-1</sup> phonons on an applied external magnetic field has been extensively studied many years ago<sup>5,7,18,19</sup> and will not be dis-

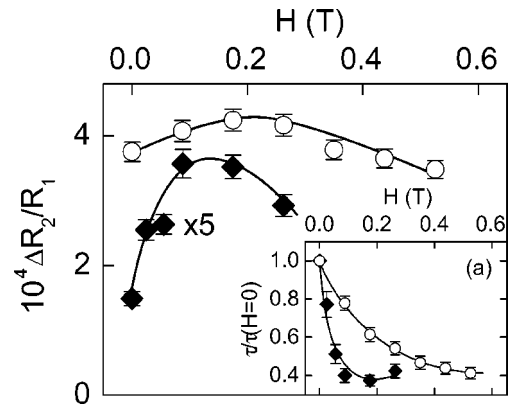


FIG. 8. Soliton-induced  $R_2$  intensity normalized to  $R_1$  as a function of applied magnetic field  $B$ , for propagation along  $c$  axis ( $\blacklozenge$ ) and  $a$  axis ( $\circ$ ). (a) Decay time  $\tau$  normalized to  $H=0$  value. Lines are guides to the eye.

cussed at this point. Most importantly, the bottleneck decay time was found to be reduced by a factor of 4 when applying a small magnetic field of  $\sim 0.1 \text{ T}$  parallel to the  $c$  axis due to the splitting of the Kramers doublets into a symmetric quartet of independent transitions. We compare here the behavior of the soliton-induced intensity upon application of small magnetic fields for both propagation directions of the acoustic strain.

The resulting luminescence intensities are shown in Fig. 8, measured at the far end of the crystal in both configurations. A significantly higher field is required to reduce the bottleneck decay time [see Fig. 8(a)] in the  $a$ -axis configuration compared to the  $c$ -axis configuration, due to the anisotropic  $g$  factor of the  $2E$  manifold. However, comparable reductions of the bottleneck decay time are obtained also in this configuration within the range of moderate fields under study. In absence of the magnetic field, we measure a bottleneck time of  $\sim 0.25 \mu\text{s}$  along the  $c$  axis and an almost two-times-as-large value along the  $a$  axis. This can be accounted for by the reduction in volume size in the on-edge  $c$ -axis configuration, reducing the escape time of resonant phonons to the bath.

Consistent with our earlier findings, the absolute  $R_2$  intensity in the two configurations in Fig. 8 differs by almost an order of magnitude. This we will denote as main observation (i). However, a new effect appears when the applied field is varied. For the case of propagation along the  $c$  axis, the  $R_2/R_1$  ratio increases by a factor of  $\sim 2.5$  when applying of a field of 0.15 T. In the  $a$ -axis configuration, however, only a small variation is observed around a mean value of  $4 \times 10^{-4}$ . The origin of this qualitative difference in the field dependence of the signal intensity will be discussed in Sec. IV C in terms of the intrinsic nonlinearity of the soliton propagation. For further discussion, we denote this magnetic-field dependence as observation (ii).

##### B. $N^*$ dependence

At this point, we explore the dependence of the signals on the concentration of excited  $\text{Cr}^{3+}$  ions  $N^*$ . For both configurations, we varied the excited-state population  $N^*$  between

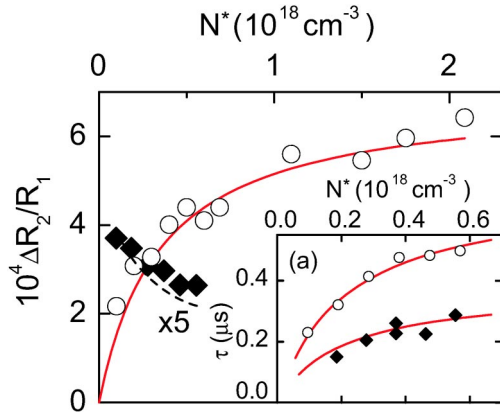


FIG. 9. (Color online) Soliton-induced  $R_2$  intensity normalized to  $R_1$  as a function of  $N^*$ , for propagation along  $c$  axis ( $\blacklozenge$ ) and  $a$  axis ( $\circ$ ). (a) Bottleneck decay time  $\tau$ . (Line/red) denotes fit using Eq. (6), (dash) denotes  $(N^*)^{-1/2}$  dependence.

0.2 and  $0.7 \times 10^{18} \text{ cm}^{-3}$ . The results of the measurements, each taken at the same spots in the crystal as in Sec. IV A, are shown in Fig. 9. Again, there is a factor of two difference in bottleneck decay time [see Fig. 9(a)] caused by the reduced zone diameter in the  $c$  axis configuration. However, *relative* increase of the bottleneck time  $\tau$  with increasing  $N^*$  is the same for both configurations and indicative of a decrease in resonant trapping time. Similar to observation (ii) in Sec. IV A, the main difference between the two configurations takes place in the amplitude behavior of the soliton-induced signal. In the  $c$ -axis configuration, the soliton-induced LA peak is seen to *decrease* slightly. In the  $a$ -axis configuration, however, the luminescence ratio *increases* by more than a factor of 2. This difference in the  $N^*$  dependence of the soliton-induced luminescence ratios we call observation (iii).

In the  $a$ -axis configuration we also measured the soliton-induced signal up to much higher values of  $N^*$ . Clearly, the signal of Fig. 9 saturates at excited-state concentrations higher than  $0.6 \times 10^{18} \text{ cm}^{-3}$ . At this point we also note the strong resemblance of the increase of the intensity with that of the bottleneck decay time in Fig. 9(a). This resemblance appears to be related to the concentration dependence of the phonon bottleneck Eq. (6) (line/red in Fig. 9), as we discuss below.

### C. Discussion

At this point we will demonstrate that the observations (i)–(iii) for the two configurations can be brought in good agreement with the model proposed in Sec. II C. First of all, the difference in absolute luminescence intensity (i) can be explained from the calculations of the spontaneously emitted energy as was shown in Fig. 3(c). Given the resonant mean free path of  $l_r \approx 2 \mu\text{m}$  for longitudinal acoustic phonons (see Appendix A) and a zone diameter of  $200 \mu\text{m}$ , the traveled distance is of the order of one hundred Beer's lengths. The energy deposited into the phonon bottleneck after  $z_j \approx 100$  [see Fig. 3(c)] is one order of magnitude less for the linear pulse than for the soliton, which agrees well with the ob-

served difference in  $R_2$  luminescence in the  $c$ - and  $a$ -axis configurations.

The magnetic-field dependence of observation (ii) reveals yet another aspect of the soliton-TLS interaction. The increase of the luminescence intensity by a factor of 2.5 in the  $c$ -axis configuration can be well understood from the point of view of available phonon modes. In the absence of refilling, a bandwidth around the absorption line will be completely depleted of phonons. The excited-state population of the electronic system is therefore limited by the available resonant phonons within the absorption bandwidth. The splitting of the electronic levels by an external magnetic field will lead to an increase of the amount of available phonons once this splitting exceeds the absorption bandwidth. In contrast, for the nonlinear solitons, the spectral absorption bandwidth is continuously replenished from other parts of the spectrum. Therefore the excited-state population is not limited by the amount of phonon modes that are available, and no dependence on magnetic field is observed.

Finally, the dependence of the luminescence ratio on the excited-state concentration  $N^*$  [observation (iii)] can be explained by the most fundamental difference found in Sec. II C, namely, that due to the nonlinear refilling, the energy is removed much faster from the soliton wave packet through spontaneous emission than from a linear strain pulse. For the linear pulse, after the first few micrometers, spontaneous emission only takes place in the wings of the resonance line shape, resulting in an electronic excitation proportional to  $(N^*)^{1/2}$  [see Eq. (2)]. As the  $R_1$  intensity is proportional to the excited-state population  $N^*$ , the normalized ratio should go as  $(N^*)^{-1/2}$ . Indeed a decrease is observed in Fig. 9(b) for the  $c$ -axis configuration.

For the soliton pulses, the energy funnelled to the phonon bottleneck is *linearly* proportional to the number of centers  $N^*$  [see Fig. 3(c)], and thus the  $R_2$ -luminescence intensity normalized to  $R_1$  should be independent of  $N^*$ . However, Fig. 9(c) shows an increasing ratio that is not predicted by the refill model. We believe that the increase of the signal with  $N^*$  along the  $a$  axis reflects the fundamental and well-studied property of the phonon bottleneck efficiency, as we explain below.

A simple rate-equation analysis shows that the incoherent  $29\text{-cm}^{-1}$  phonon energy extracted from the solitons is redistributed equally over the phonon bath and the electronic centers, yielding a ratio of the electronic populations according to

$$\frac{N_{2\bar{A}}}{N_{\bar{E}}} = p_{2\bar{A}} \frac{N^*}{N^* + \rho \Delta \nu}, \quad (6)$$

with  $\rho \Delta \nu$  the Debye density of states around the 0.87 THz phonon frequency. In this balance, the critical parameter is the bandwidth  $\Delta \nu$  over which the coherent electronic polarization tail is converted to phonons. We find good agreement with the experimentally observed behavior for a bandwidth  $\Delta \nu \approx 10 \text{ GHz}$  [line in Fig. 9(c)] and an excited-state occupation number  $p_{2\bar{A}}$  of  $7 \times 10^{-3}$ . This bandwidth is higher than the inhomogeneous linewidth of the transition of 0.3 GHz,<sup>20</sup>

but is in the ball park of the Kramers-doublet splitting in the applied magnetic field.

The resemblance of the behavior of the bottleneck decay time with the  $N^*$  dependence of the  $R_2/R_1$  ratio in Figs. 9(a) and 9(b) is strongly connected to the detailed balance between spin and phonon baths. The ratio  $\rho\Delta\nu/N^*$ , appearing on the right side of Eq. (6) reflects the relative “trapping” ratio  $\tau_r/T_1$ ,<sup>7</sup> with  $\tau_r=l_r/c_0$  the resonant absorption time and  $T_1$  the spontaneous-emission lifetime. This ratio describes the fraction of time that a resonant energy-quantum resides in the phonon state. The phonon “escape” time  $\tau$ , constituted of spatial diffusion and anharmonic decay, is slowed down with increasing  $N^*$  by exactly the same ratio as the luminescence intensity in Eq. (6), due to the increasing amount of time the energy quantum spends in the electronic state, where it is immune to phonon-escape processes.

## V. CONCLUSIONS AND PROSPECTS

In conclusion, we have studied the interaction of ultrashort strain solitons and the electronic  $\bar{E}(^2E)-2\bar{A}(^2E)$  transition along the ruby  $a$  and  $c$  axes. The directional component in the observed luminescence signal demonstrates the presence of 0.87-THz phonons in the soliton train. The ruby phonon spectrometer can thus be used as a detector for ultrashort strain solitons, yielding information complementary to the Brillouin scattering method of Ref. 2.

The remarkable properties of the soliton-induced luminescence for propagation along the  $a$  axis have been explained by the model of nonlinear refilling of the spectral absorption dip by the walk off of the fast soliton from its induced dipole radiation. The observation of a signal exclusively near the far end of the crystal in the  $c$ -axis configuration has been explained by the suppression of electron-phonon interaction along this axis. Diffusive scattering and mode conversion of phonons at the surface effectively enhance the interaction with the  $\text{Cr}^{3+}$  ions, resulting in the observed behavior.

The behavior of the soliton signal as a function of magnetic field and excited-state concentration were found to be consistent with the presented model based on the nonlinear properties of the solitons. The two crystallographic configurations could be used to demonstrate the difference between linear and nonlinear propagation of strain packets through the resonant two-level medium.

In the future, the two-level medium may be used as a tool for the manipulation or even amplification of coherent strain pulses. Instead of preparing the two-level systems in the ground state, one can consider direct inversion via strong optical pumping of the  $2\bar{A}$  level. The transmission of an ultrashort strain pulse through the inverted medium will then result in a coherent release of energy from the electronic state into the longitudinal acoustic strain field. The Bloch angle would undergo exponential growth characterized by the resonant Beer’s length. However the amplification process is limited by spontaneous decay, leading to a cooperation length  $c_0T_1$  of ten micrometers for the  $\bar{E}(^2E)-2\bar{A}(^2E)$  transition. Depending on the degree of inversion reached, an amplification of the resonant component by two or three orders of magnitude may be achieved and  $\pi$  pulses could be

reached. A much longer cooperation length of millimeters could be obtained by inversion of the Kramers-split  $\bar{E}$  level,<sup>18</sup> and would allow the construction of a phonon laser.

## ACKNOWLEDGMENTS

The authors wish to thank A. V. Akimov for his contribution to the experiments and for many helpful discussions. P. Jurrius and C. R. de Kok are acknowledged for their technical assistance. This work was supported by The Netherlands Foundation “Fundamenteel Onderzoek der Materie (FOM)” and the “Nederlandse Organisatie voor Wetenschappelijk Onderzoek (NWO).”

## APPENDIX A: TRANSITION MATRIX ELEMENT AND RESONANT PHONON MEAN FREE PATH

In this appendix we estimate the matrix element of the  $\bar{E}(^2E)-2\bar{A}(^2E)$  phonon transition, for the configuration of uniaxial, longitudinal strain along the  $a$  axis, which experimentally yields the strongest interaction between the longitudinal phonons and the two-level medium. Additionally, we give an for the mean free path for transverse and longitudinal acoustic phonons in the two-level medium.

The problem of phonon-induced transitions in the  $^2E$  state was addressed by Blume *et al.*<sup>21</sup> and Geschwind *et al.*<sup>22</sup> in the context of deriving a quantitative expression for the spontaneous emission lifetime  $T_1$  from the  $2\bar{A}(^2E)$  state to the metastable  $\bar{E}(^2E)$  level in case of spin-flip and nonspin-flip transitions. In this derivation, static strain data on the  $R_1$  and  $R_2$  line positions<sup>23</sup> were used to estimate the off-diagonal matrix elements involved in the phonon transition.

In their derivation, it was found that only the trigonal,  $T_2$ -symmetric vibrations contribute to the transition probability when taking into account first order mixing in the electronic wave functions of states within the  $t_2^3$  configuration. These vibrations connect through the trigonal  $^2T_2$  electronic doublet, giving rise to a matrix element for nonspin-flip transitions of the form

$$\langle \bar{E}'_{+-} | H_{T_2} | 2\bar{A}'_{+-} \rangle = -\frac{2K}{\Delta} V(T_2)_{s_+} = Q_{s_+}, \quad (\text{A1})$$

where  $Q=(2K/\Delta)V(^2T_2)$  denotes the actual matrix element of the transition, while the parameter  $s_+$  denotes the component of the applied strain in the corresponding  $x_+$  mode of the  $^2T_2$  basis. Here  $K$ ,  $\zeta$  are the trigonal field and spin-orbit parameters, respectively,<sup>21</sup> and  $\Delta=6734 \text{ cm}^{-1}$  is the energy splitting between the  $^2E$  and  $^2T_2$  electronic levels. The reduced matrix element  $\bar{V}(^2T_2)$  has been obtained from experimental data for the  $\bar{E}-2\bar{A}$ -level splitting for strain along the  $c$  axis. The strain-induced change in  $R_2-R_1$  splitting was measured to be  $0.55 \text{ cm}^{-1}/\text{GPa}$  in static strain experiments,<sup>23,24</sup> and  $0.44 \text{ cm}^{-1}/\text{GPa}$  in shock wave experiments.<sup>25</sup> Following the argumentation by Blume *et al.*,<sup>21</sup> this yields a value for  $V(^2T_2) \approx 2.4 \times 10^4 \text{ cm}^{-1}$  per unit of trigonal strain. The magnitude of  $s_+$  can be derived simply from the uniaxial strain  $s$  by transforming to a trigonal basis, which along the  $a$  axis gives

$$s_+(T_2) = \frac{1 - i\sqrt{3}s}{4} \frac{s}{3}, \quad (\text{A2})$$

where the complex nature of the strain is a consequence of the mathematical construction. For applied stress along the  $c$  axis, the transformation to trigonal strain components yields an  $s_+$  which is exactly zero,<sup>23,25</sup> which explains the absence of the  $R_2$  luminescence induced by the longitudinal phonons in this crystallographic direction, as observed in Ref. 7 and by us in this paper. A uniaxial strain  $s$  along the  $a$  axis will contain a trigonal component  $|s_+| = q_+s$ , with  $q_+ \approx 0.29$  the reduction factor obtained from Eq. (A2). Given the known values for the material constants<sup>26</sup>  $\zeta \approx 180 \text{ cm}^{-1}$  and  $K \approx 250 \text{ cm}^{-1}$ , we obtain an estimate for the matrix element for nonspin-flip transitions of  $\hbar\chi_0 = |Qq_+| \approx 450 \text{ cm}^{-1}$ .

From the matrix element, one can estimate the spontaneous emission lifetime and the resonant phonon mean free path. This was done by Blume *et al.* and resulted in a reasonable value of the spin-flip transition of 30 ns and a ratio of spin-flip to nonspin-flip transition of about 60. However, later experiments<sup>6</sup> showed that this ratio is only about 15. This discrepancy may be due to the variation in values for the constants  $\zeta$  and  $K$ , that determine this ratio. Furthermore, the cubic approximation for the phonon density of states is probably another weak link in the expression for the relaxation rates. If we consider the error in the spin-flip rate to be caused by this phonon density of states, we may still identify the spin-flip matrix element with the diagonal element obtained from the line shift data,<sup>22</sup> and with the factor of 15 between the experimentally obtained lifetimes, we then arrive at an approximation of the nonspin-flip matrix element  $Q$  which is about 4 times larger than the spin-flip element of  $\sim 200 \text{ cm}^{-1}$ . Combined with the factor  $q_+$  this yields a Rabi frequency of  $\hbar\chi_0 \approx 250 \text{ cm}^{-1}$ . We have chosen to use this

lower estimate in the calculations of the excited population in this paper.

We now present some estimates for the absorption of resonant  $29\text{-cm}^{-1}$  phonons in the resonant medium consisting of excited  $\text{Cr}^{3+}$  ions. The mean free path  $\bar{l}_r$  for the resonant phonons in a two-level medium excited to a concentration  $N^*$  can be derived along different lines. Our first attempt starts from the rate equations governing the equilibrium of spin and phonon baths, that are on speaking terms through the crystal-field interaction. From the principle of detailed balance for the electronic and phonon subsystems, an important relation can be derived between the spontaneous emission lifetime and the resonant absorption time  $\tau_r = \bar{l}_r/c_0$ , given by<sup>7</sup>

$$\tau_r/T_1 = D(\omega)\Delta\omega/N^*, \quad (\text{A3})$$

with the Debye density of states  $D(\omega)\Delta\omega = V\omega^2\Delta\omega/2\pi c_0^3 \approx 3 \times 10^{16} \text{ cm}^{-3}$ . This directly provides an estimate for the resonant mean free path of  $\bar{l}_r \approx 0.2 \mu\text{m}$  for TA phonons at the typical  $N^* = 10^{18} \text{ cm}^{-3}$ .

Another approach for the determination of the absorption length  $\bar{l}_r$  involves the solution to the coupled equations for the electronic system and the elastic continuum. Derivations for the coupled spin-phonon system have been obtained by Jacobsen and Stevens,<sup>27</sup> Shiren,<sup>8</sup> and recently by Tilstra *et al.*<sup>28</sup> Shiren derived an explicit expression for the absorption coefficient, given by

$$\bar{l}_r^{-1} = \frac{2\pi N^* \chi_0^2 \omega T_1}{\rho \hbar c_0^3}. \quad (\text{A4})$$

Note the analogy with the optical case,<sup>11</sup> when replacing  $\epsilon_0$  by  $\rho c_0^2$ , and the dipole moment  $\mu$  by  $\chi_0$ . Equation (A4) results in an estimate of  $\bar{l}_r \approx 2.4 \mu\text{m}$  for LA and  $\bar{l}_r \approx 0.4 \mu\text{m}$  for TA phonons, at  $N^* = 10^{18} \text{ cm}^{-3}$ . These results compare well with those of the detailed balance equation, indicating that our estimate of the Rabi frequency is very reasonable.

\*Electronic address: J.I.Dijkhuis@phys.uu.nl

<sup>1</sup>H.-Y. Hao and H. J. Maris, Phys. Rev. B **64**, 064302 (2001).

<sup>2</sup>O. L. Muskens and J. I. Dijkhuis, Phys. Rev. Lett. **89**, 285504 (2002).

<sup>3</sup>O. L. Muskens and J. I. Dijkhuis, Phys. Rev. B **70**, 104301 (2004).

<sup>4</sup>K. F. Renk and J. Deisenhofer, Phys. Rev. Lett. **26**, 764 (1971).

<sup>5</sup>J. I. Dijkhuis, A. van der Pol, and H. W. de Wijn, Phys. Rev. Lett. **37**, 1554 (1976).

<sup>6</sup>J. E. Rives and R. S. Meltzer, Phys. Rev. B **16**, 1808 (1977).

<sup>7</sup>A. A. Kaplyanskii and S. A. Basun, in *Nonequilibrium Phonons in Nonmetallic Crystals*, edited by W. Eisenmenger and A. A. Kaplyanskii (North Holland, Amsterdam, 1986), p. 373.

<sup>8</sup>N. S. Shiren, Phys. Rev. B **2**, 2471 (1970).

<sup>9</sup>J.-Y. Prieur, J. Joffrin, and K. Lassman, Physica B **316-317**, 125 (2002).

<sup>10</sup>O. L. Muskens, A. V. Akimov, and J. I. Dijkhuis, Phys. Rev. Lett. **92**, 035503 (2004).

<sup>11</sup>L. Allen and J. H. Eberly, *Optical Resonance and Two-Level Atoms* (General Publishing Company, Toronto, 1987), 2nd ed.

<sup>12</sup>D. C. Burnham and R. Y. Chiao, Phys. Rev. **188**, 667 (1969).

<sup>13</sup>M. Crisp, Phys. Rev. A **1**, 1604 (1970).

<sup>14</sup>F. T. Arecchi and E. Courtens, Phys. Rev. A **2**, 1730 (1970).

<sup>15</sup>J. D. Jackson, *Classical Electrodynamics*, 3rd ed. (Wiley, New York, 1998).

<sup>16</sup>O. L. Muskens, S. Purushothaman, A. V. Akimov, and J. I. Dijkhuis, J. Lumin. **108**, 281 (2004).

<sup>17</sup>J. M. Winey, Y. M. Gupta, and D. E. Hare, J. Appl. Phys. **90**, 3109 (2001).

<sup>18</sup>J. I. Dijkhuis, K. Huibregtse, and H. W. de Wijn, Phys. Rev. B **20**, 1835 (1979).

<sup>19</sup>R. J. G. Goossens, J. I. Dijkhuis, and H. W. de Wijn, Phys. Rev. B **32**, 7065 (1985).

<sup>20</sup>M. J. van Dort, J. I. Dijkhuis, and H. W. de Wijn, Phys. Rev. B **41**, 8657 (1990).

<sup>21</sup>M. Blume, R. Orbach, A. Kiel, and S. Geschwind, Phys. Rev. **139**, A314 (1965).

<sup>22</sup>S. Geschwind, G. E. Devlin, R. L. Cohen, and S. R. Chinn, Phys. Rev. **137**, A1087 (1965).

<sup>23</sup>A. L. Schawlow, *Advances in Quantum Electronics* (Columbia

- University Press, New York, 1961), p. 50.
- <sup>24</sup>E. Feher and M. D. Sturge, Phys. Rev. **172**, 244 (1968).
- <sup>25</sup>S. M. Sharma and Y. M. Gupta, Phys. Rev. B **43**, 879 (1991).
- <sup>26</sup>R. M. Macfarlane, J. Chem. Phys. **47**, 2066 (1967).
- <sup>27</sup>E. H. Jacobsen and K. W. H. Stevens, Phys. Rev. **129**, 2036 (1963).
- <sup>28</sup>L. G. Tilstra, A. F. M. Arts, and H. W. de Wijn, Phys. Rev. B **68**, 144302 (2003).